BME Horizon

Science Exploration

Open Access Research Article

Study on mechanical properties and mix ratio optimization of granulated blast furnace slag based composite materials for solidifying inorganic softened sludge from power plants

Chaoyi Ma[1,3], Chao Liu[1,2,3], Chao Zhu[1,3], Xin Guo[1,3], Yifei Wang[1,3], Wenxuan Zhu[1,3], Huawei Liu[1,*]

[1]School of Civil Engineering, Xi'an University of Architecture and Technology, Xi'an 710055, Shaanxi, China.
[2]School of Science, Xi'an University of Architecture & Technology, Xi'an 710055, Shaanxi, China.
[3]Key Lab of Structural Engineering and Earthquake Resistance, Ministry of Education (XAUAT), Xi'an 710055, Shaanxi, China.

***Correspondence to:** Huawei Liu, School of Civil Engineering, Xi'an University of Architecture and Technology, Xi'an 710055, Shaanxi, China. E-mail: liuhuawei@xauat.edu.cn

Received: December 18, 2025 **Accepted:** February 25, 2026 **Published:** March 04, 2026

Cite this article: Ma C, Liu C, Zhu C, Guo X, Wang Y, Zhu W, et al. Study on mechanical properties and mix ratio optimization of granulated blast furnace slag based composite materials for solidifying inorganic softened sludge from power plants. J Build Des Environ. 2026;4:2025142. https://doi.org/10.70401/jbde.2026.0032

Abstract

This study addresses the challenges of solidifying high-moisture, high-alkalinity inorganic softening sludge (ISS) by utilizing alkali-activated slag-based cementitious materials. The research investigated strength evolution via unconfined compressive strength tests, while X-ray diffraction and scanning electron microscopy were employed to analyze phase composition and microstructural changes. Furthermore, response surface methodology was utilized to optimize mix proportions and explore interaction mechanisms. Results indicate that granulated blast furnace slag is the primary strength contributor, whereas fly ash and sodium silicate exhibit nonlinear effects. Microscopic analysis reveals that changes in raw material ratios influence strength development by regulating the formation of products such as calcium aluminosilicate hydrate (C-A-S-H) and sodium aluminosilicate hydrate (N-A-S-H). Optimization results from response surface methodology show that, when sodium hydroxide dosage is fixed at 2.5%, the optimal dosages for granulated blast furnace slag, fly ash, and sodium silicate are 30.65%, 29.98%, and 6.96%, respectively, achieving a 7-day unconfined compressive strength of 5.38 MPa. Furthermore, significant interactions exist between granulated blast furnace slag and fly ash, as well as between fly ash and sodium silicate. This study provides a theoretical basis for the resource utilization of ISS in road base materials.

Keywords: Curing agent, compressive strength, inorganic softening sludge, response surface method, mix ratio

1. Introduction

Thermal power plants serve as critical hubs for energy supply, supporting economic and social development while simultaneously facing severe pressure regarding solid waste disposal. Among various solid wastes, inorganic softening sludge (ISS) exhibits distinct characteristics, including high alkalinity, high calcium ion content, and high water content. The treatment of ISS has become a critical environmental bottleneck restricting the green transformation of the industry. Traditional disposal methods, such as landfilling, stockpiling, and incineration, are not only plagued by low efficiency and low resource utilization rates but are also prone to generating leachate, thereby causing secondary pollution[1-3]. In light of this, exploring an efficient and environmentally friendly technical pathway for the large-scale resource utilization of ISS is of great significance for promoting the clean transformation of the thermal power industry and achieving sustainable development goals[4].

In recent years, utilizing solidified sludge as a road base material has emerged as a promising strategy for sludge treatment due to its combined economic viability and engineering applicability[5,6]. Existing studies indicate that cement and admixtures can effectively solidify municipal sludge or soft soil into materials with sufficient strength to meet road construction requirements[7-10]. The use of nano-modification and low-carbon supersulfated cement can efficiently cure dressed dimensions[11]. Building on this, the application of alternative solidifying agents, such as rice husk ash, granulated blast furnace slag (GBFS), magnesium oxide, fly ash (FA), and metakaolin, has further enhanced the solidification efficacy of municipal sludge and soft soil[12-15]. Notably, solidification systems

© The Author(s) 2026. This is an Open Access article licensed under a Creative Commons Attribution 4.0 International License (https://creativecommons.org/licenses/by/4.0/), which permits unrestricted use, sharing, adaptation, distribution and reproduction in any medium or format, for any purpose, even commercially, as long as you give appropriate credit to the original author(s) and the source, provide a link to the Creative Commons license, and indicate if changes were made.

based on alkali-activated materials have demonstrated particularly outstanding performance[16-18]. Feng *et al.*[19] reviewed the mechanical properties and solidification mechanisms of alkali-activated cementitious materials solidified sludge and analyzed the influence of sludge type, alkali activator type, precursor type and dosage on the unconfined compressive strength (UCS) of alkali-activated cementitious materials solidified sludge. The use of sodium silicate (SS) as an activator can significantly enhance the solubility of GBFS, thereby significantly improving its compressive strength[20]. The synergistic interaction between GBFS and FA facilitates a more comprehensive alkali-activation process, where the simultaneous formation of C-A-S-H and N-A-S-H gels leads to a denser geopolymeric matrix and enhanced structural integrity of the solidified soil[21-23]. Optimizing the binary blend of GBFS and FA significantly improves the unconfined compressive strength of stabilized soils by refining the pore structure and accelerating the hydration kinetics under alkaline environments[24-26]. Alkali activators composed of SS and sodium hydroxide (SH) accelerate the dissolution rates of silicon and aluminum in GBFS and FA, promoting gel formation[27].

However, existing research has primarily focused on the solidification characteristics of municipal sludge or soft soil[28-31]. Due to the high moisture content, high calcium ion content, and high alkalinity of ISS, its physical and chemical properties differ significantly from traditional sludge, making direct application of existing findings challenging. Although alkaline activation is applicable to urban sludge/soft soil, and existing research has demonstrated that the inherent alkalinity within the sludge can substitute for some external alkaline activators, thereby reducing material costs, and that its abundant calcium ions can swiftly engage in alkaline activation reactions, endowing the solidified sludge with high mechanical properties[32], the application of alkaline activation in ISS with high moisture content, high calcium levels, and high pH has yet to be thoroughly investigated. The potential of harnessing the inherent alkalinity of ISS as a resource represents a novel research avenue. Accordingly, this study utilizes slag-based alkali-activated materials for the synergistic solidification of ISS. Through single-factor experiments, the intrinsic relationship between the dosage of the slag-based cementitious agent and UCS was investigated. Coupled with X-ray diffraction (XRD) analysis to elucidate the mechanism of product evolution, the mix proportion of the solidifying agent was optimized using response surface methodology (RSM), and the significant interaction mechanisms between raw material dosages were explored. This study provides a theoretical basis for the resource utilization of ISS in road base materials.

2. Materials and Methods

2.1 Materials

The physicochemical properties of the ISS used in the experiments are presented in Figure 1 and Table 1. X-ray fluorescence analysis indicates that the predominant oxides are CaO, MgO, and SiO_2. The sludge exhibits a plasticity index of 20.9 and a liquidity index of 1.22, characterizing it as a high-liquid-limit soil in a flow-plastic state. Notably, the ISS possesses a pH of 10.1. Although this alkalinity is insufficient to independently trigger the pozzolanic reaction of slag (which typically requires pH > 12), it serves as a supplementary alkaline source, effectively reducing the demand for external sodium hydroxide compared to neutral sludge. As shown in Figure 2, the particle size distribution is narrow, with a mean particle size centered around 10 μm.

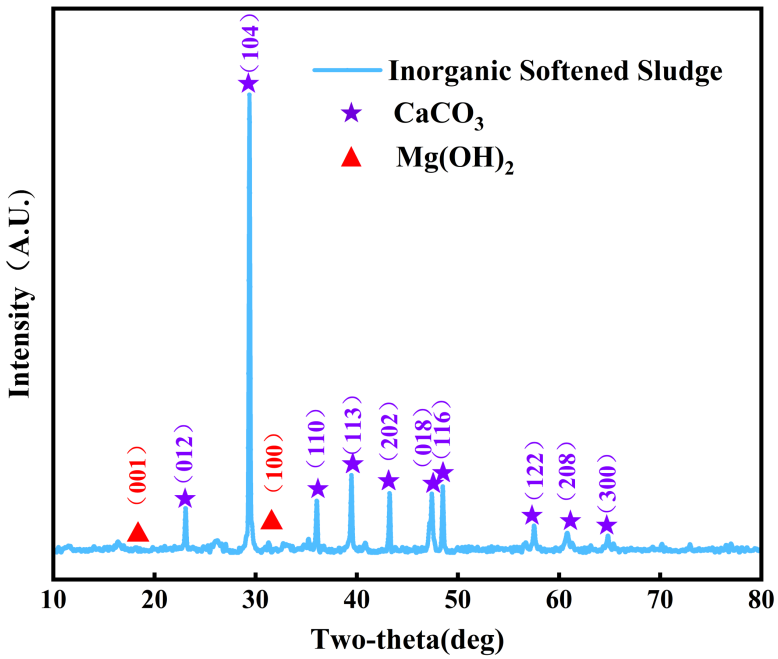


Figure 1. Main components of ISS. ISS: inorganic softening sludge.

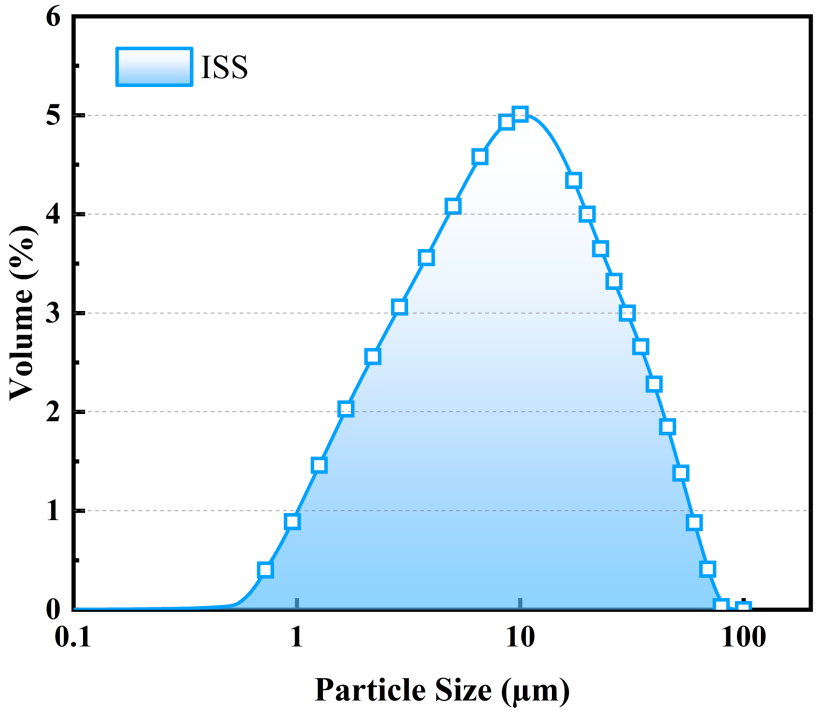


Figure 2. Particle size distribution of ISS. ISS: inorganic softening sludge.

Table 1. Main chemical components of the material.

Compound	CaO	MgO	SiO_2	Fe_2O_3	SO_3	Al_2O_3
ISS	77.991	6.605	5.48	3.76	3.492	0.921
GBFS	34.00	6.01	34.50	1.03	1.64	17.70
FA	8.92	1.55	46.17	7.90	1.91	26.68

ISS: inorganic softening sludge; GBFS: granulated blast furnace slag; FA: fly ash.

Previous research has shown that GBFS and SS exhibit effective solidification performance for high-water-content dredged sludge[19], and that the hydration products of FA can enhance the binding strength between soil particles[33]. Based on the high water content, high calcium ion content, and high alkalinity of ISS, as well as the plasticity and flowability indicators of the sludge[19], GBFS, FA, SS, and SH were selected as raw materials for the solidifying agent. The chemical compositions of ISS, GBFS, and FA are listed in Table 1.

2.2 Mix ratio

Experiments were designed with ISS, GBFS, FA, and SS in the proportions specified in Table 2. The base dosage of SH was 4% of the total mass of the curing agent, and it was varied in gradients of 0.5% within the range of 2% to 4%[34]. The dosages of each component are detailed in Table 2.

Table 2. Mix proportions of the solidifying agent components (wt%).

Variable factor	Group	ISS (%)[a]	GBFS (%)[a]	FA (%)[a]	SS (%)[a]	SH (%)[b]
GBFS content	SP-1	10	2	3	1	4
	SP-2	10	2.5	3	1	4
	SP-3	10	3	3	1	4
	SP-4	10	3.5	3	1	4
	SP-5	10	4	3	1	4
FA content	FA-1	10	3	2	1	4

	FA-2	10	3	2.5	1	4
	FA-3	10	3	3	1	4
	FA-4	10	3	3.5	1	4
	FA-5	10	3	4	1	4
SS content	SS-1	10	3	3	0	4
	SS-2	10	3	3	0.5	4
	SS-3	10	3	3	1	4
	SS-4	10	3	3	1.5	4
	SS-5	10	3	3	2	4
SH content	SH-1	10	3	3	1	2
	SH-2	10	3	3	1	2.5
	SH-3	10	3	3	1	3
	SH-4	10	3	3	1	3.5
	SH-5	10	3	3	1	4

[a]: the addition amount of ISS, GBFS, FA, and SS is displayed as their weight ratio; [b]: the amount of SH added is displayed as a percentage of the total weight of the curing agent; ISS: inorganic softening sludge; GBFS: granulated blast furnace slag; FA: fly ash; SS: sodium silicate; SH: sodium hydroxide; SP: slag powder.

2.3 Sample preparation and testing

To simulate extreme field conditions, a moisture content of 70% was adopted as the experimental baseline, reflecting the upper limit of the typical 50%–70% range observed in practical engineering. The sample preparation workflow is depicted in Figure 3. ISS was oven-dried to a constant weight at 65 °C, comminuted via a jaw crusher, and sieved through a 2 mm square-hole mesh. The retained fraction was re-processed to ensure 100% passing. Components were weighed according to the mix design, and the process from hydration to casting into 40 mm cubic molds was rigorously executed within 10 minutes. After 24 hours of ambient curing, the specimens were demolded and transferred to a standard curing chamber (20 ± 2 °C, RH ⩾ 90%). UCS tests were conducted at 3, 7, and 28 days, and the average value of three replicates was reported.

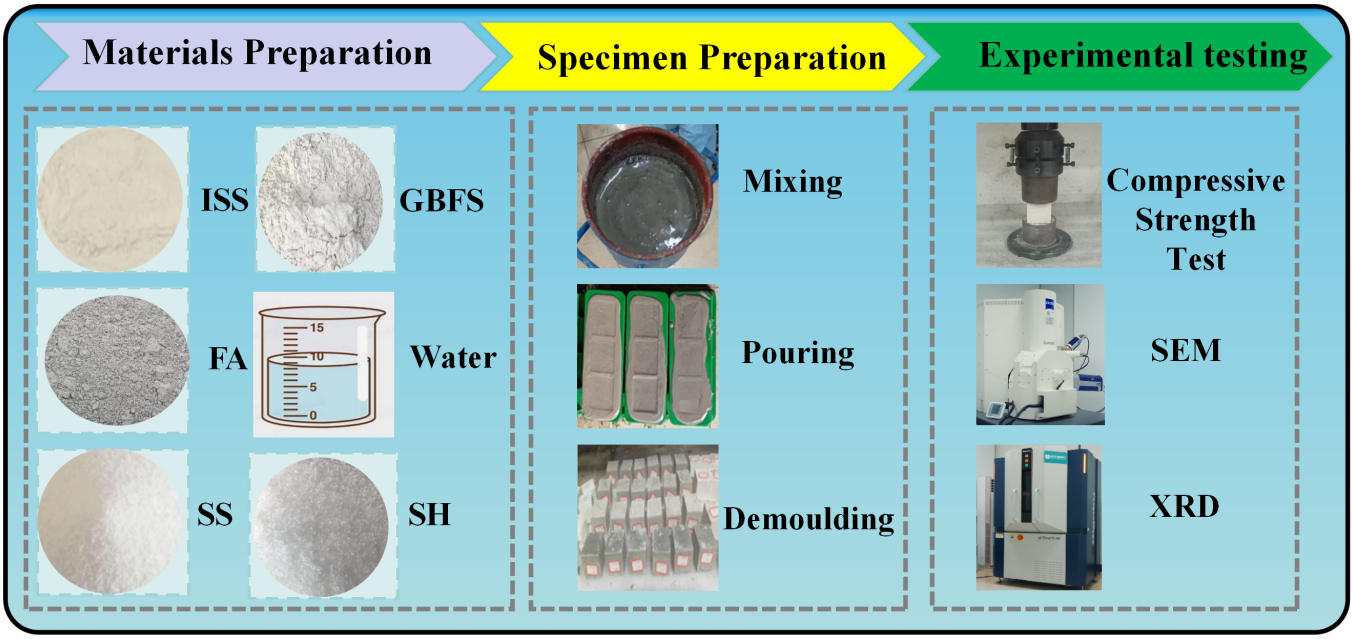


Figure 3. Sample preparation and testing equipment. ISS: inorganic softening sludge; FA: fly ash; SS: sodium silicate; GBFS: granulated blast furnace slag; SH: sodium hydroxide; SEM: scanning electron microscopy; XRD: X-ray diffraction.

3. Single Factor Test Results

3.1 Unconfined compressive strength

Figure 4, Figure 5, Figure 6, and Figure 7 illustrate the distinct effects of solidifying agent component dosages on the UCS of the solidified sludge. For the GBFS-based system, the UCS exhibits a significant positive correlation with dosage. At a GBFS dosage of 40%, the compressive strengths at 3, 7, and 28 days reach 6.03 MPa, 7.60 MPa, and 9.11 MPa, respectively. However, when the GBFS dosage exceeds 35%, the growth in 28-day strength tends to plateau. The influence of FA dosage on strength follows a trend of increasing and then decreasing. The 28-day strength reaches a maximum of 7.79 MPa at an FA dosage of 35%. The effect of SS dosage on UCS exhibits a biphasic characteristic: when the SS dosage is below 10%, the 28-day strength declines with increasing dosage, reaching a minimum of 7.2 MPa at 10%. Subsequently, the strength increases with dosage, recovering to 8.18 MPa at both 15% and 20% dosages, representing an increase of approximately 14%. Regarding SH dosage, inconsistent trends were observed; specifically, while early-age strength increases when the dosage ranges from 3.5% to 4%, the 28-day strength decreases. Nevertheless, the overall fluctuation in strength across all curing ages remains within 1 MPa, suggesting that, compared to other raw materials, the influence of SH dosage on strength is relatively minor.

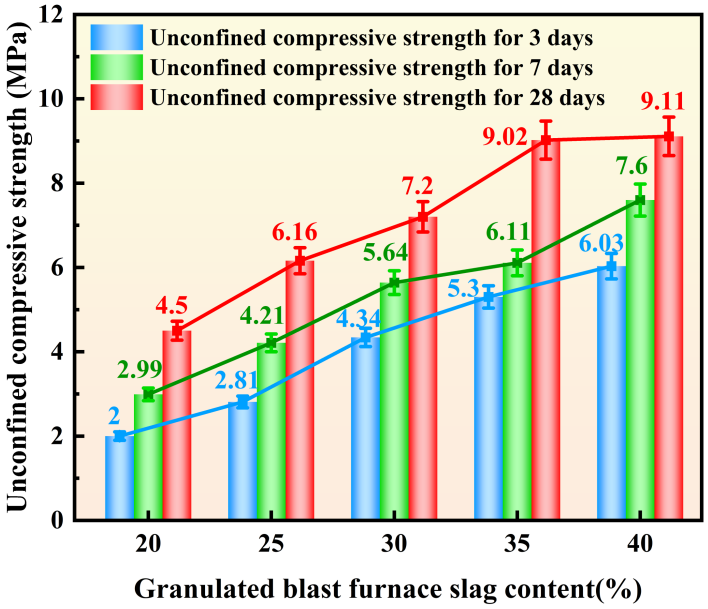


Figure 4. Effect of GBFS dosages on the UCS of solidified sludge. GBFS: granulated blast furnace slag; UCS: unconfined compressive strength.

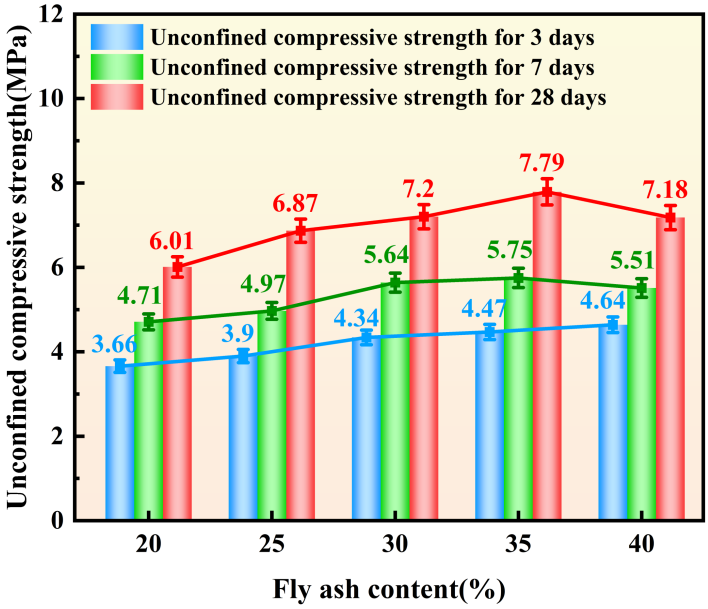


Figure 5. Effect of FA dosages on the UCS of solidified sludge. FA: fly ash; UCS: unconfined compressive strength.

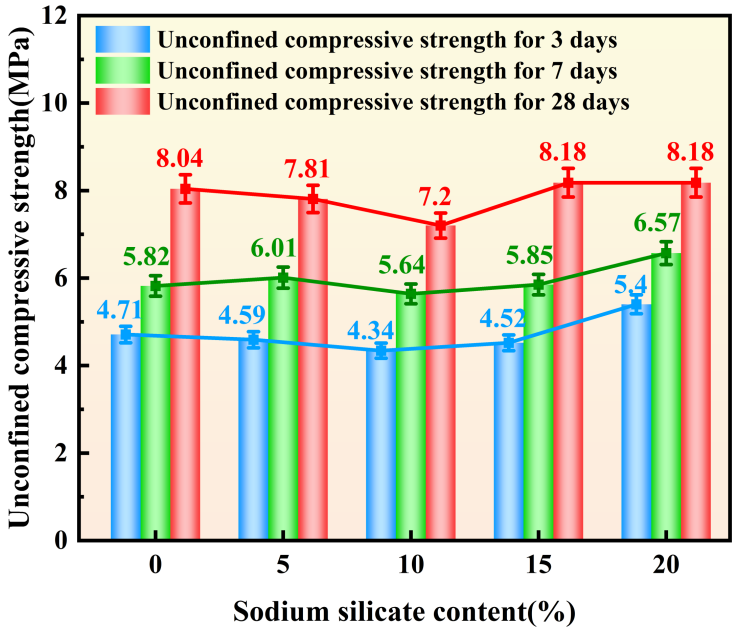


Figure 6. Effect of SS dosages on the UCS of solidified sludge. SS: sodium silicate; UCS: unconfined compressive strength.

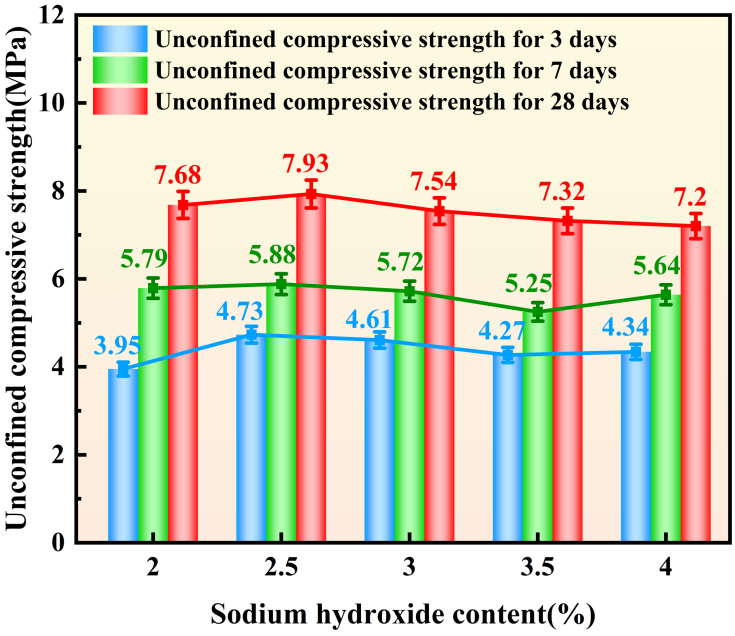


Figure 7. Effect of SH dosages on the UCS of solidified sludge. SH: sodium hydroxide; UCS: unconfined compressive strength.

3.2 Curing mechanism

The XRD patterns in Figure 8 reveal the phase evolution characteristics of the solidified sludge under different mix ratios. The results for Group SP-5 exhibit characteristic features of alkali-activated products. It should be noted that the calcium aluminosilicate hydrate (C-A-S-H) gel formed in this system is largely amorphous and poorly crystalline, making it difficult to detect as sharp diffraction peaks in XRD. Instead, its presence is inferred from the broad diffuse halo and the consumption of crystalline precursor phases, consistent with the dense gel structures observed in SEM images. This is attributed to the alkali-activated reaction, where Ca^{2+} ions from the ISS and GBFS consume a significant amount of free water to generate C-A-S-H gel, which provides strength[35]. At a curing age of 28 days, the $CaCO_3$ peak intensifies significantly while the SiO_2 peak diminishes. This indicates that when the Ca^{2+} concentration exceeds the demand for the alkali-activated reaction, the excess Ca^{2+} forms $Ca(OH)_2$, which subsequently reacts with atmospheric CO_2 to generate $CaCO_3$. This carbonation process is accompanied by volume expansion, which inhibits late-age strength development and reasonably explains the plateau in 28-day strength observed in Groups SP-4 and SP-5.

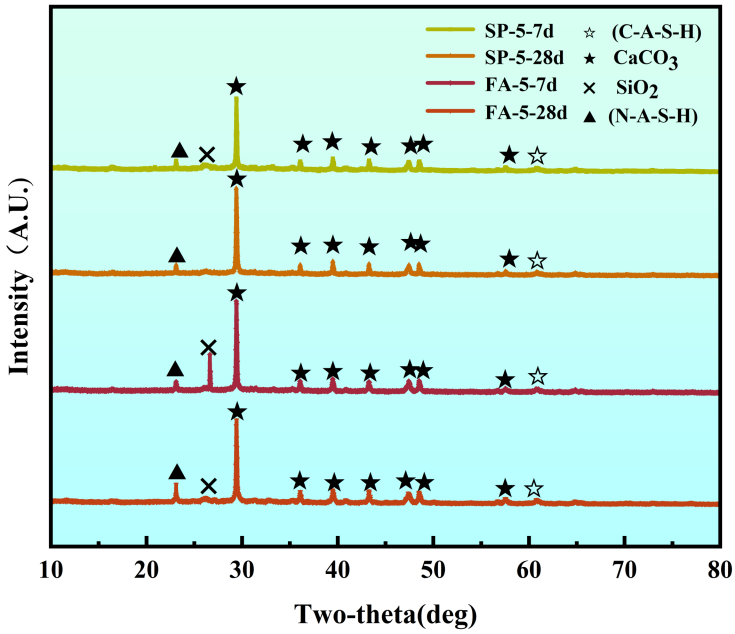


Figure 8. XRD results. XRD: X-ray diffraction; FA: fly ash; SP: slag powder.

The dosages of FA and SS influence the type of hydration products by regulating the Ca^{2+}/Si^{4+} ratio within the system. As shown in Figure 4, Group FA-5 displays a prominent SiO_2 peak at 7 days, whereas a distinct sodium aluminosilicate hydrate (N-A-S-H) peak emerges at 28 days. At low FA dosages, sufficient Ca^{2+} rapidly reacts with SiO_4^{4-} released from FA under alkaline conditions to form C-A-S-H gel, significantly enhancing early-age strength. Conversely, high FA dosages reduce the Ca/Si ratio, promoting the transformation of reaction products into lower-strength N-A-S-H, which consequently weakens the solidified matrix.

Regarding SS dosage, the strength of the solidified sludge initially decreases as the dosage increases. This occurs because the Si^{4+} in SS is more reactive than that in FA and participates preferentially in the reaction, thereby lowering the system's Ca/Si ratio and favoring the formation of low-strength N-A-S-H. As the SS dosage continues to increase, the pH of the system decreases, promoting the dissolution of Al_2O_3 and SiO_2 from FA to generate AlO_4^{5-} and SiO_4^{4-}. These ions then combine with Ca^{2+} in the sludge. This process facilitates the connectivity of pores and the collapse of large-to-medium pores, reducing total pore volume. Simultaneously, newly generated gels (C/N-A-S-H) interlock and cement the sludge particles into a dense network structure, thereby recovering and improving the strength. The microstructural evolution directly correlates with the biphasic trend in Figure 6. The initial strength drop is due to the formation of low-strength N-A-S-H caused by a reduced Ca/Si ratio, while the subsequent recovery is driven by the pore-filling effect of excess silicate species.

The alkaline environment provided jointly by SH and ISS is crucial for activating the reactivity of GBFS and FA. An appropriate amount of SH promotes the dissolution of active calcium, silicon, and aluminum, increasing the yield of C-A-S-H gel. However, excessively high SH dosage has a dual effect: while it aids in the depolymerization of active substances, the excess Na^+ provided by SH and SS can lead to the precipitation of carbonate phases such as Gaylussite ($Na_2Ca(CO_3)_2{\cdot}5H_2O$), hindering the formation of strength-giving gels[36]. Consequently, the compressive strength decreases, although the overall variation is minor.

4. Response Surface Methodology Optimization Results

4.1 Model analysis

Based on the results of the single-factor experiments, the dosage ranges for GBFS, FA, and SS were established as 20%-40%, 20%-40%, and 0%-20%, respectively. Given that SH is a strong alkali activator associated with high energy consumption and carbon emissions[37], and that excessive addition yields limited strength improvements, its dosage was minimized in alignment with the principles of green, low-carbon, and sustainable development. Consequently, following preliminary trials and an environmental benefit assessment, the SH dosage was fixed at 2.5% of the total solidifying agent mass[34] and was treated as a constant rather than a variable in the subsequent optimization.

To further optimize the mix proportions of GBFS, FA, and SS, the 7-day UCS was selected as the response variable[34]. A three-factor (X_1, X_2, X_3), three-level (-1, 0, 1) experimental scheme was designed using the Box-Behnken Design method within the Design-Expert software. Subsequently, the preparation, curing, and strength testing of the solidified sludge were conducted according to this protocol. The final experimental results and response surface analysis are presented in Table 3.

Table 3. Response surface analysis results.

Run	GBFS content (wt%)	FA content (wt%)	SS content (wt%)	UCS for 7d (MPa)
1	40.00	20.00	10.00	5.98
2	30.00	30.00	10.00	5.32
3	30.00	30.00	10.00	5.32
4	40.00	30.00	20.00	7.17
5	40.00	30.00	0.00	6.78
6	20.00	30.00	20.00	3.19
7	30.00	40.00	20.00	6.45
8	30.00	20.00	0.00	3.69
9	30.00	20.00	20.00	4.77
10	40.00	40.00	10.00	9.2
11	20.00	40.00	10.00	4.68
12	20.00	20.00	10.00	2.82
13	30.00	30.00	10.00	5.32
14	30.00	30.00	10.00	5.32
15	30.00	30.00	10.00	5.32
16	30.00	40.00	0.00	7.11
17	20.00	30.00	0.00	2.96

GBFS: granulated blast furnace slag; FA: fly ash; SS: sodium silicate; UCS: unconfined compressive strength.

Following the analysis of the RSM experimental data, a quadratic polynomial regression model was fitted to correlate the dosage changes with the target response value. From Table 4, it can be observed that the Prob > *F* value of the model is less than 0.01, which indicates that the response surface regression model reaches an extremely significant level with high fitting accuracy and can be used for subsequent optimization design. The Prob > *F* value of the Lack of Fit is greater than 0.05, indicating that the Lack of Fit is not significant. Meanwhile, the Prob > *F* values of the linear terms A, B, and C are less than 0.01, demonstrating that the dosages of GBFS, FA, and SS have an extremely significant influence on the 7 d UCS. The Prob > *F* values of the interaction terms AB and BC are also less than 0.01, indicating that the interaction effects between GBFS dosage and FA dosage, as well as between FA dosage and SS dosage, exert an extremely significant influence on the 7 d UCS. By comparing the magnitude of *F* values, the order of factors affecting 7-day UCS from strong to weak is determined as GBFS content, FA content, and SS content.

Table 4. Analysis of variance for regression models.

	Sum of		Mean	*F*	*p*-value
Source	Squares	df	Square	Value	Prob > *F*
Model	45.19	9	5.02	5,131.01	< 0.0001
A-GBFS content	29.95	1	29.95	30,609.72	< 0.0001
B-FA content	12.95	1	12.95	13,237.72	< 0.0001
C-SS content	0.14	1	0.14	138.16	< 0.0001
AB	0.46	1	0.46	472.53	< 0.0001
AC	0.0064	1	0.0064	6.54	0.0377
BC	0.76	1	0.76	773.47	< 0.0001
A^2	0.018	1	0.018	18.18	0.0037

B^2	0.73	1	0.73	741.04	< 0.0001
C^2	0.22	1	0.22	227.61	< 0.0001
Residual	0.0068	7	0.0009	/	/
Lack of Fit	0.0068	3	0.0022	2.17	0.2342
Pure Error	0.000	4	0.000	/	/
Cor Total	45.20	16	/	/	/

GBFS: granulated blast furnace slag; FA: fly ash; SS: sodium silicate.

As shown in Table 5, the multiple correlation coefficient R-Squared is close to 1, indicating a strong correlation between the observed and predicted values. The values of Adjusted R-Squared and Predicted R-Squared are relatively high, with a difference of less than 0.2, demonstrating that the regression model possesses good predictive capability and consistency. The coefficient of variation is less than 10%, confirming the high reliability and reproducibility of the experiments. Furthermore, the Adequate Precision is greater than 4, indicating a desirable signal-to-noise ratio. Collectively, these metrics verify that the fitted regression equation satisfies the requirements of statistical testing.

Table 5. Statistical analysis of regression equation errors.

Std. Dev.	0.031	R-Squared	0.9998
Mean	5.38	Adj R-Squared	0.9997
C.V.%	0.58	Pred R-Squared	0.9976
PRESS	0.11	Adeq Precision	267.377

C.V.: coefficient of variation.

The quadratic multiple regression equation for the 7 d UCS response value (Y_7) is shown as Eq. (1).

$$Y_7 = 0.3625 + 0.1265A - 0.18B + 0.1775C + 0.0034AB + 0.0004AC - 0.00435BC - 0.00065A^2 + 0.0041B^2 - 0.0023C^2 \quad (1)$$

As shown in Figure 9, Figure 10, and Figure 11, the data points in the normal probability plot of residuals generally cluster along the straight line, indicating that the residuals follow a normal distribution. The plot of residuals versus predicted values shows a random distribution on both sides of the zero line without any specific pattern, suggesting constant variance. Furthermore, the predicted values and actual values align closely with the diagonal line. These results demonstrate that the model fitted by RSM possesses high adequacy and reliability.

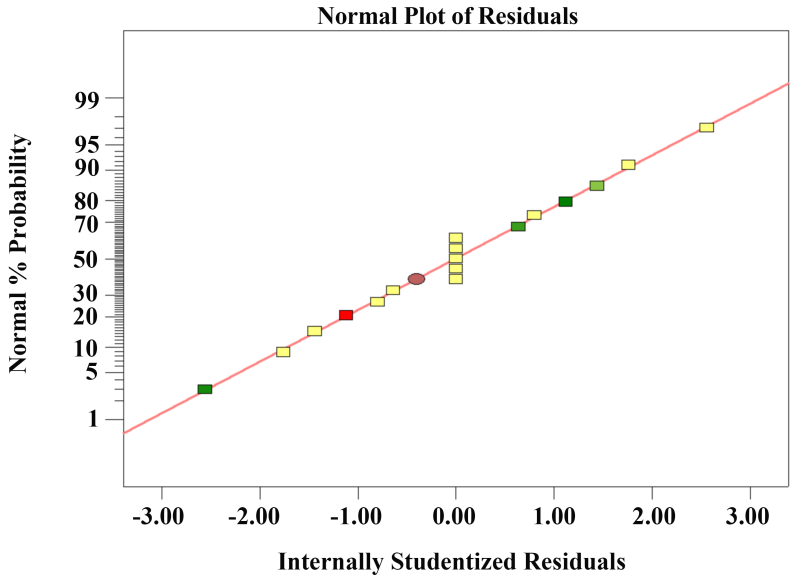


Figure 9. Normal probability distribution of residuals.

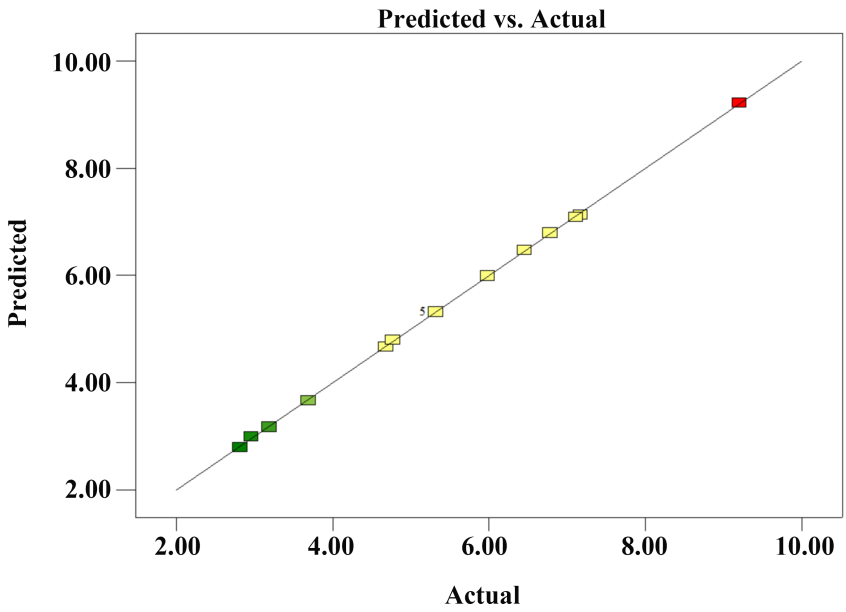


Figure 10. Distribution of residuals and predicted values.

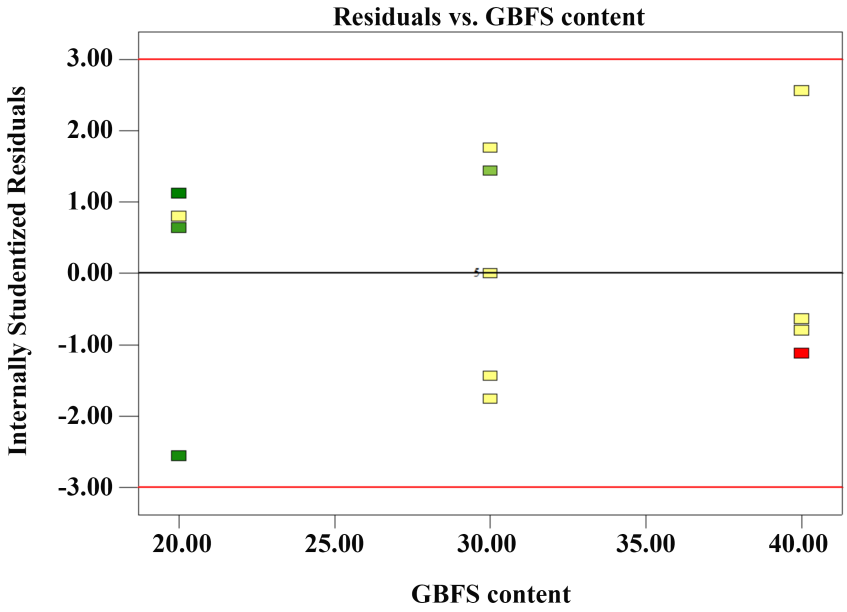


Figure 11. Distribution of predicted and actual values. GBFS: granulated blast furnace slag.

4.2 Interaction analysis

Based on the fitted quadratic polynomial model, 3D response surface plots and corresponding contour plots were generated to visualize the pairwise interactions, with the third factor held constant at its central level.

Figure 12 and Figure 13 illustrate the interaction between GBFS and FA. The 3D surface exhibits a steep gradient as the dosages increase, indicating that the interaction between GBFS and FA exerts a significant influence on the 7-day UCS. Notably, the response surface curve is steeper along the GBFS axis than along the FA axis, demonstrating that GBFS dosage has a more pronounced impact on strength development than FA dosage.

In contrast, as shown in Figure 14 and Figure 15, the contour lines for the GBFS and SS interaction are uniformly distributed and approximately circular. This morphology indicates that the interaction effect between GBFS and SS is not statistically significant. However, the steeper slope observed along the GBFS axis compared to the SS axis confirms that the influence of GBFS dosage is dominant over that of SS dosage.

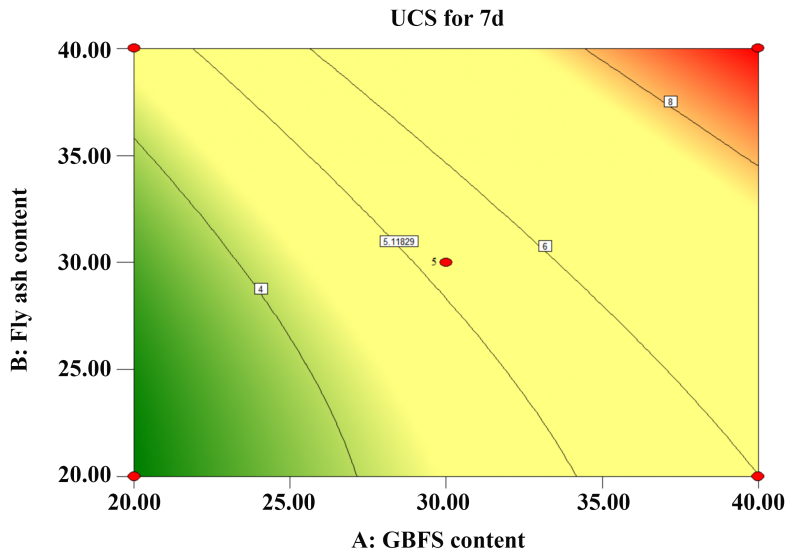


Figure 12. Contour map of GBFS and FA. GBFS: granulated blast furnace slag; FA: fly ash; UCS: unconfined compressive strength.

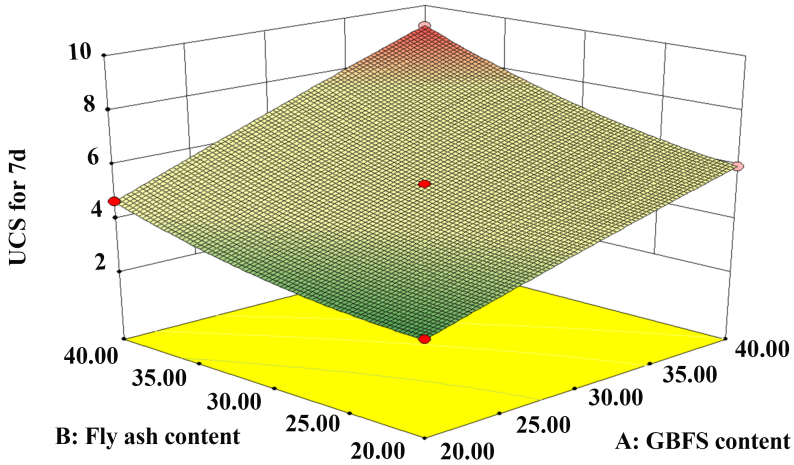


Figure 13. 3D diagram of GBFS and FA. GBFS: granulated blast furnace slag; FA: fly ash; UCS: unconfined compressive strength.

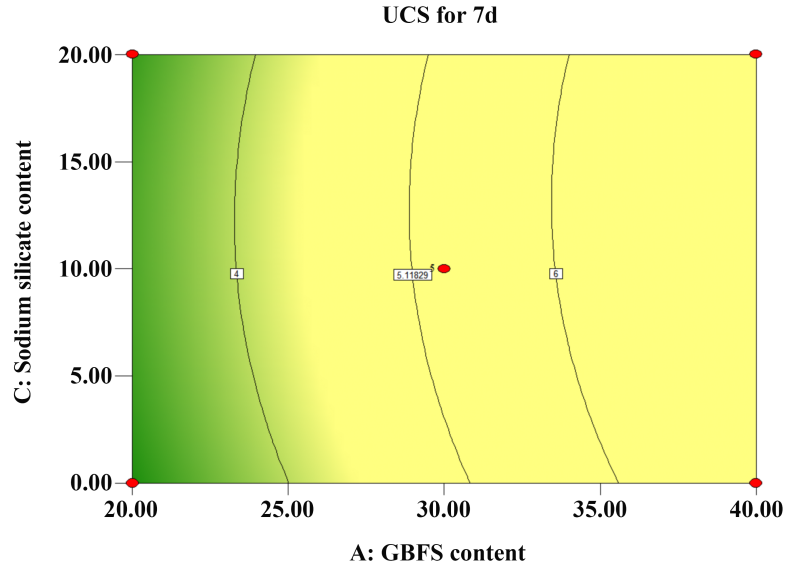


Figure 14. Contour map of GBFS and SS. GBFS: granulated blast furnace slag; SS: sodium silicate; UCS: unconfined compressive strength.

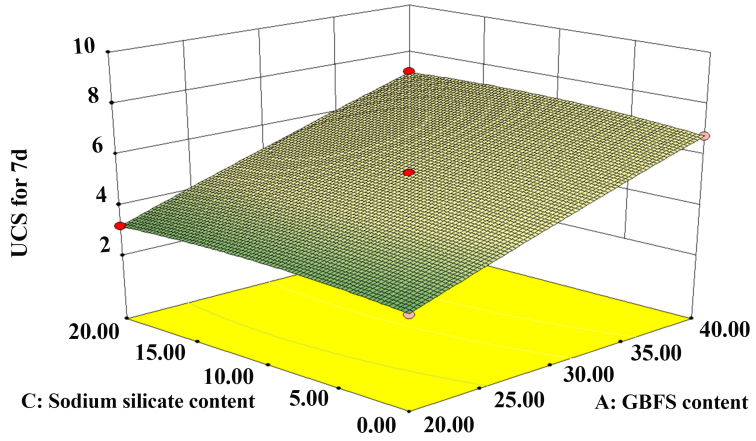


Figure 15. 3D diagram of GBFS and SS. GBFS: granulated blast furnace slag; SS: sodium silicate; UCS: unconfined compressive strength.

Figure 16 and Figure 17 present the interaction between FA and SS. The response surface shows distinct curvature, and the contour lines are densely distributed, suggesting a significant interaction effect on the 7-day UCS. Additionally, the slope along the FA axis is steeper than that along the SS axis, indicating that FA dosage exerts a greater influence on the solidified sludge strength than SS dosage.

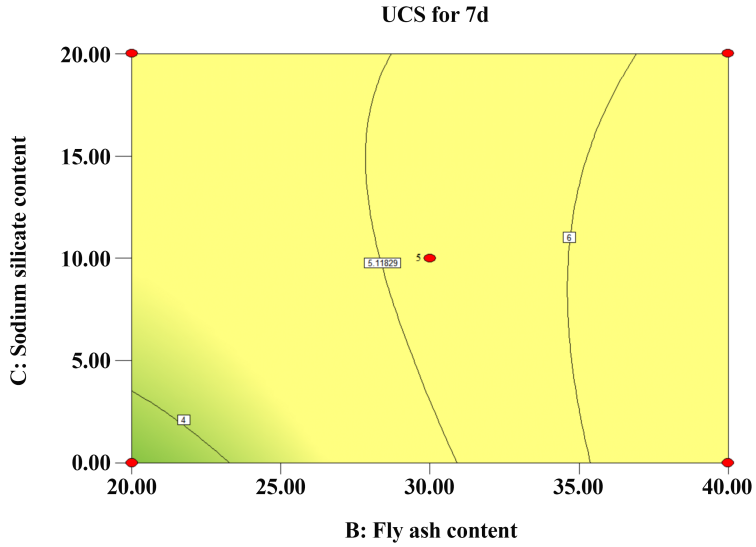


Figure 16. Contours of FA and SS. FA: fly ash; SS: sodium silicate; UCS: unconfined compressive strength.

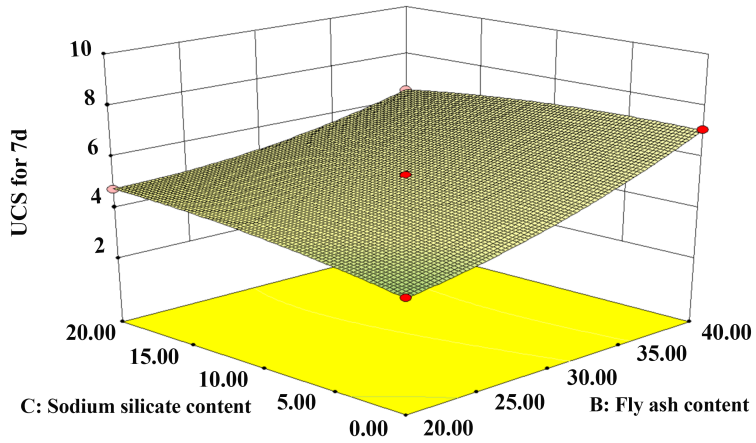


Figure 17. 3D diagram of FA and SS. FA: fly ash; SS: sodium silicate; UCS: unconfined compressive strength.

4.3 Significant interaction mechanism

The synergistic interaction between GBFS and FA exerts a significant regulatory effect on the 7-day UCS of the solidified sludge. Figure 18a,b display the SEM images of Group SP-5 at curing ages of 3 and 7 days, respectively. In Figure 18a, numerous dense agglomerated structures are observed. This is attributed to the high Ca^{2+} content inherent in the ISS, combined with the addition of GBFS, which further elevates the system's Ca/Si ratio. In the highly alkaline environment, Si^{4+} and Al^{3+} released from GBFS and FA undergo pozzolanic reactions to generate substantial amounts of amorphous calcium aluminosilicate hydrate (C-A-S-H) gel. The primary hydration reaction can be described as follows.

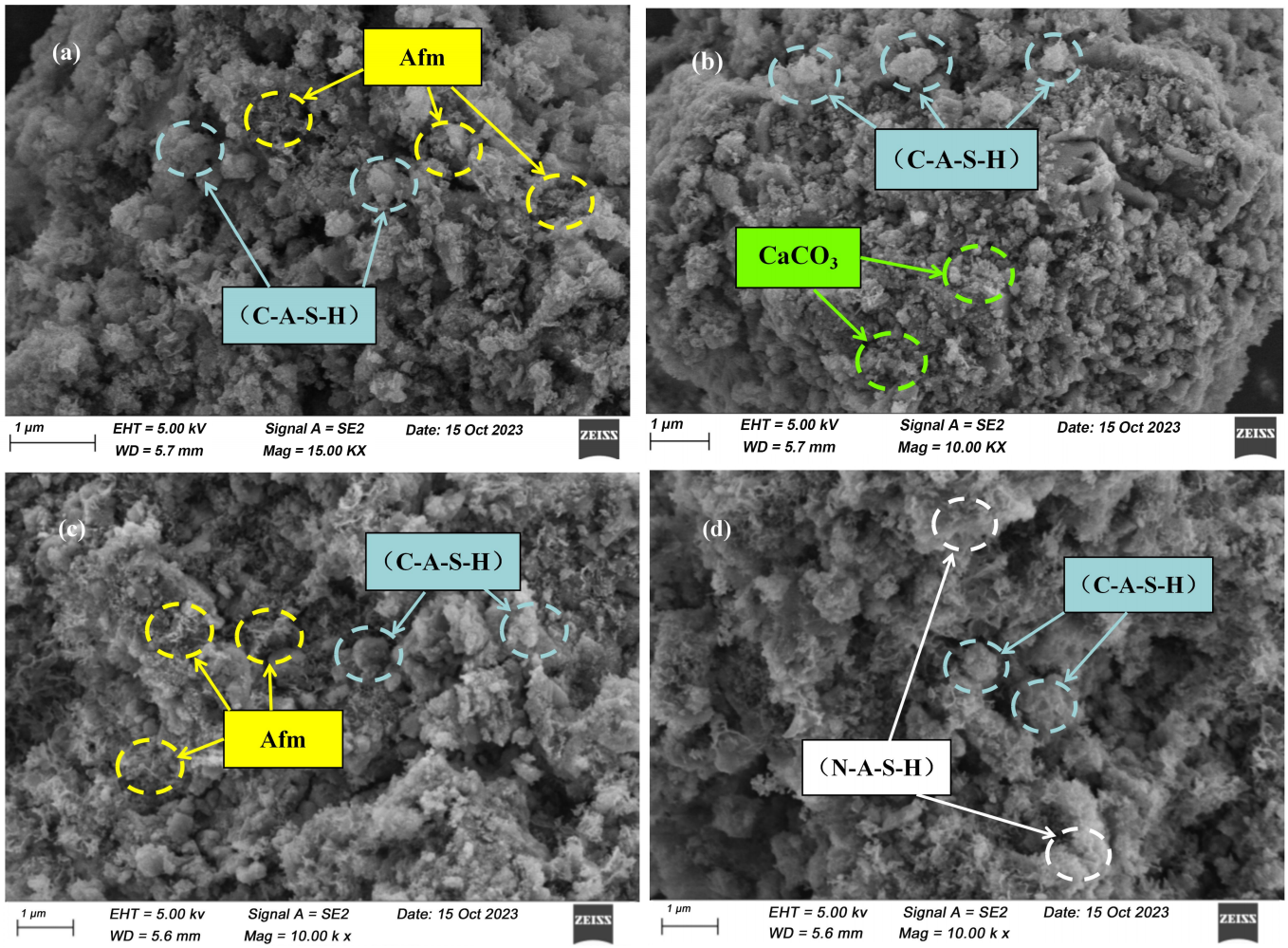


Figure 18. SEM images of SP-5 group and FA-5 group. (a) SEM image of SP-5 at 3 days; (b) SEM image of SP-5 at 7 days; (c) SEM image of FA-5 at 3 days; (d) SEM image of FA-5 at 7 days. SEM: scanning electron microscopy; SP: slag powder; FA: fly ash.

$$x\mathrm{Ca}^{2+} + \mathrm{SiO}_3^{2-} + 2y\mathrm{AlO}_2^- + 2(x-y-1)\mathrm{OH}^- + (n-x+y+1)\mathrm{H_2O} \rightarrow x\mathrm{CaO}\cdot\mathrm{SiO_2}\cdot y\mathrm{Al_2O_3}\cdot n\mathrm{H_2O} \quad (2)$$

This gel not only effectively encapsulates ISS particles but also adsorbs free water, forming a dense cementitious structure that significantly reduces porosity and provides core support for compressive strength. Meanwhile, residual Ca^{2+} reacts with OH^- to form $Ca(OH)_2$ crystals. This process accelerates the hydration of GBFS and FA, and the subsequent carbonation of $Ca(OH)_2$ with atmospheric CO_2 generates fine-grained $CaCO_3$. These carbonates fill the pores of the solidified matrix, further densifying the microstructure and enhancing early-age strength.

However, in Figure 18b, although the number of fine agglomerates increases, localized loose regions appear. This occurs because, as the hydration progresses to 7 days, the carbonation of excess $Ca(OH)_2$ intensifies. The resulting volume expansion from $CaCO_3$ formation leads to the development of microcracks within the solidified matrix. Additionally, the excessive Ca^{2+} results in an overly high Ca/Si ratio, which reduces the crystallinity of the C-A-S-H gel and weakens its cementitious performance. The combined effect of these factors leads to a deceleration in the strength growth rate at the 7-day curing age.

The interaction between FA and SS also significantly influences the 7-day UCS. Figure 18c,d present the SEM images of Group FA-5 at

3 and 7 days. Figure 18c clearly shows the coexistence of numerous acicular (needle-like) structures and dense agglomerates. During the early reaction stage, SS rapidly dissociates to provide a high concentration of free Si^{4+}, which combines with Ca^{2+} and Al^{3+} to form agglomerated C-A-S-H gel. Simultaneously, the high Ca^{2+} content reacts with Al^{3+} and SO_4^{2-} to generate acicular monosulfate-type calcium aluminate hydrate (AFm) crystals.

$$4Ca^{2+} + 2AlO_2^- + SO_4^{2-} + 4OH^- + 10H_2O \rightarrow 3CaO \cdot Al_2O_3 \cdot CaSO_4 \cdot 12H_2O \tag{3}$$

These crystals intersperse within the gel, forming an interwoven "gel-crystal" network that significantly improves early compressive strength.

In Figure 18d, the number of acicular structures diminishes, while the proportion of flocculent agglomerates increases, correlating with a decline in the strength growth rate. The core reason is that, as FA continues to react, the release of Si^{4+} and Al^{3+} gradually lowers the system's Ca/Si ratio. Consequently, the original C-A-S-H gel transforms into low-calcium products, and the Na^+ from SS facilitates the formation of flocculent sodium aluminosilicate hydrate (N-A-S-H) gel.

$$2nNa^+ + 2nAlO_2^- + 4nSiO_3^{2-} + 6nH_2O \rightarrow nNa_2O \cdot nAl_2O_3 \cdot 4nSiO_2 \cdot 2nH_2O + 8nOH^- \tag{4}$$

This N-A-S-H gel possesses lower cementitious strength and a looser structure. Furthermore, the formation of acicular AFm crystals ceases due to Ca^{2+} depletion. This reduction in microstructural compactness explains the slowdown in strength development at the 7-day curing age.

4.4 Numerical optimization and experimental verification

To ensure the engineering applicability of the solidified sludge, the mix proportion was optimized to balance mechanical performance and material efficiency. Based on the regression model established in Eq. (1), a mathematical optimization model was constructed using the desirability function approach.

The optimization objective is to maximize the 7-day unconfined compressive strength Y_{7d} within the feasible experimental domain. The independent variables are the dosages of GBFS (A), FA (B), and SS (C). The optimization problem can be mathematically described as a constrained nonlinear programming problem, as shown in Eq. (5):

$$\begin{cases} \text{Maximize } Y_{7d} = f(A, B, C) \\ \text{Subject to:} \\ 20 \le A \le 40 \\ 20 \le B \le 40 \\ 0 \le C \le 20 \end{cases} \tag{5}$$

where $f(A, B, C)$ corresponds to the quadratic polynomial regression equation derived in Section 4.1. The constraints define the boundary conditions of the component dosages (wt%) based on the single-factor experimental design.

To solve this optimization problem, the desirability function method D was employed. The response variable Y_{7d} is transformed into an individual desirability value d_i, which ranges from 0 to 1. The transformation function is defined as follows:

$$d_i = \begin{cases} 0 & Y_i \le Y_{min} \\ \left(\frac{Y_i - Y_{min}}{Y_{target} - Y_{min}}\right)^w & Y_{min} < Y_i < Y_{target} \\ 1 & Y_i \ge Y_{target} \end{cases} \tag{6}$$

$$D^2 = (d_1^{w_1} d_2^{w_2} \cdots d_i^{w_i})^{\frac{1}{\sum w_i}} \tag{7}$$

Y_{min} is the lower limit (3MPa) of the response specified by the standard[33]. Y_{target} is the target maximum strength (set to the experimental maximum of 9.20 MPa), and w is the weight factor (set to 1 for linear optimization). The algorithm seeks the vector of variables (A, B, C) that maximizes the composite desirability.

Using the optimization module in Design-Expert software to solve the above equations, the optimal point in the design space was located. The analysis yielded the optimal mix proportion: 30.65% GBFS, 29.98% FA, and 6.96% SS. Under these conditions, the predicted desirability is maximal, corresponding to a theoretical 7-day UCS of 5.38 MPa.

To validate the mathematical accuracy of the established model, the optimal variable values were substituted into the quadratic regression equation (Eq. (1)) derived in Section 4.1. The calculation process for the predicted strength Y_{7d} is as follows:

$$\begin{aligned} Y_{7d} = {} & \beta_0 + \beta_1(30.65) + \beta_2(29.98) + \beta_3(6.96) + \beta_{12}(30.65 \times 29.98) + \beta_{13}(30.65 \times 6.96) \\ & + \beta_{23}(29.98 \times 6.96) + \beta_{11}(30.65)^2 + \beta_{22}(29.98)^2 + \beta_{33}(6.96)^2 = 5.38\text{MPa} \end{aligned} \tag{8}$$

β_0 through β_{33} are the regression coefficients obtained from the ANOVA analysis (Eq. (1)). The calculated theoretical value of 5.38 MPa represents the maximum potential strength predicted by the model under these specific conditions.

Experimental verification was subsequently conducted to assess the reliability of this prediction. Three parallel specimens were prepared using the optimized mix ratio. As shown in Figure 19, the experimental results yielded an average 7-day UCS of 5.38 ± 0.05 MPa, with individual values of 5.33, 5.38, and 5.43 MPa. This high degree of consistency confirms that the quadratic polynomial model constructed in this study possesses excellent predictive accuracy and can effectively guide the mix design of ISS solidification.

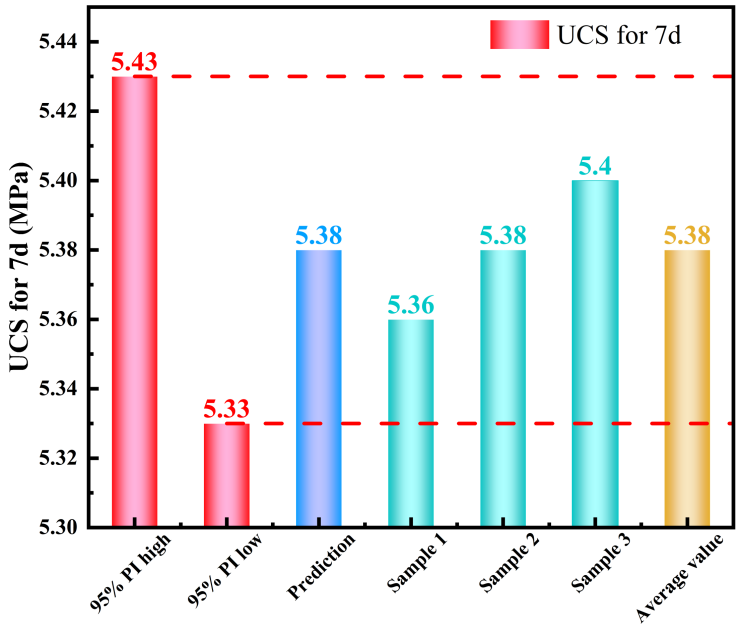


Figure 19. Predictive analysis and experimental results. UCS: unconfined compressive strength.

5. Conclusion

(1) GBFS is the primary contributor to strength. FA and SS exhibit non-linear biphasic effects due to their regulation of the system's Ca/Si ratio, which dictates the transition between high-strength C-A-S-H and lower-strength N-A-S-H gels.

(2) Significant interactions exist between GBFS and FA. The high alkalinity of ISS supplements the activation process, where Ca^{2+} from ISS and GBFS reacts with silicate/aluminate species to form a dense "gel-crystal" network. However, excessive carbonation at late stages (forming $CaCO_3$) can induce microcracks, slightly hindering long-term strength gain.

(3) RSM optimization determined the optimal dosages to be 30.65% GBFS, 29.98% FA, and 6.96% SS (with 2.5% SH), yielding a 7-day UCS of 5.38 ± 0.05 MPa, which matches the predicted value.

This study primarily focused on mechanical performance and short-term microstructural evolution. Future research should investigate the long-term durability of the solidified ISS, specifically its resistance to wet-dry cycles and the leaching behavior of heavy metals, to fully validate its environmental safety as a road base material.

Declarations

Acknowledgments

Gemini 3.0 Pro was used only to assist with language polishing and did not contribute to the generation of the research content.

Authors contribution

Ma C: Data curation, methodology, investigation, writing-original draft, writing-review & editing.
Liu C: Funding acquisition,
Zhu C: Methodology.
Guo X: Investigation, supervision.
Wang Y, Zhu W: Investigation.
Liu H: Investigation, writing-review & editing.

Conflicts of interest

Huawei Liu is a Youth Editorial Board Member of *Journal of Building Design and Environment*. The other authors declare no conflicts of interest.

Ethical approval

Not applicable.

Consent to participate

Not applicable.

Consent for publication

Not applicable.

Availability of data and materials

Data supporting the findings of this study are available from the corresponding author upon reasonable request.

Funding

The work was supported by Shaanxi Qinchuangyuan "Scientist + Engineer" Team Construction Project (Grant No. 2023KXJ-242), Shaanxi Provincial Natural Science Basic Research Program (Grant No. 2025JC-YBMS-550), and Shaanxi Provincial Education Department Youth Innovation Team Project (Grant No. 24JP095).

Copyright

© The Author(s) 2026.

References

1. Bianchini A, Bonfiglioli L, Pellegrini M, Saccani C. Sewage sludge drying process integration with a waste-to-energy power plant. Waste Manag. 2015;42:159-165. [DOI][PubMed]
2. Zhang Y, Li Y, Cheng M, Yao A, Jing Z. A novel approach to return sludge to nature: Hydrothermal conversion of full sludge components into humic acid and functional minerals. J Clean Prod. 2025;508:145562. [DOI]
3. Deng S, Yu Y, Yao L, Liu H, Xu J, Huo H, et al. Energy efficiency analysis of a rotating-drum dryer using hot steel balls for converter sludge. Case Stud Therm Eng. 2023;49:103389. [DOI]
4. Zhao Y, Liu H, Wei G, Zhu Y, Zhang S, Liu Z, et al. Effect of sewage sludge separation pretreatment on the performance of sludge-based porous ceramsite. Constr Build Mater. 2025;466:140343. [DOI]
5. Li Y, Liu X, Li Z, Ren Y, Wang Y, Zhang W. Preparation, characterization and application of red mud, fly ash and desulfurized gypsum based eco-friendly road base materials. J Clean Prod. 2021;284:124777. [DOI]
6. Wang H, Xu K, Dong L, Sun D. Global trends and perspectives in soil stabilization/solidification technologies: A three-decade bibliometric analysis focused on heavy metal remediation and sustainable applications. J Environ Chem Eng. 2026;14(2):121279. [DOI]
7. Zou Z, Qin Y, Zhang T, Tan K. Enhancing road performance of lead-contaminated soil through biochar-cement solidification: An experimental study. J Environ Manage. 2023;348:119315. [DOI][PubMed]
8. Shen J, Xiao J, Li S. Mechanism and mechanical property of recycled solidified excavated soil by cement and geopolymer. Constr Build Mater. 2025;483:141597. [DOI]
9. Feng S, Zhang G, Ren Y. Properties and microstructure of soil solidified by titanium slag-flue gas desulfurized gypsum-Portland cement composites as solidifiers. Constr Build Mater. 2024;438:137061. [DOI]
10. Yao Q, Tu Y, Yang J, Zhao M. Hybrid XGB model for predicting unconfined compressive strength of solid waste-cement-stabilized cohesive soil. Constr Build Mater. 2024;449:138242. [DOI]
11. Lang L, Wang D, Chen B, Li D, Gu L. Efficient stabilization of dredged sediment by combining nano-modification and low-carbon supersulfated cement. J Rock Mech Geotech Eng. 2025. [DOI]
12. Sun Z, Chen W, Zhao R, Malik N, Yin J, Chen Y. Investigation on solidified/stabilized behavior of marine soil slurry by lime-activated incinerated sewage sludge ash-ground granulated blast furnace slag under multifactor conditions. J Rock Mech Geotech Eng. 2024;16(12):5264-5277. [DOI]
13. Abdila SR, Al Bakri Abdullah MM, Ahmad R, Rahim SZA, Rychta M, Wnuk I, et al. Evaluation on the mechanical properties of ground granulated blast slag (GGBS) and fly ash stabilized soil via geopolymer process. Materials. 2021;14(11):2833. [DOI]
14. Renjith R, Robert D, Setunge S, Costa S, Mohajerani A. Optimization of fly ash based soil stabilization using secondary admixtures for sustainable road construction. J Clean Prod. 2021;294:126264. [DOI]
15. Tan YZ, Ke R, Ming HJ. Improving the durability of organic matter in cement-treated sludge using metakaolin and lime. Mar Georesour

Geotechnol. 2021;39(3):293-301. [DOI]
16. Wang Z, Yuan Q, Zhou C, Lu Z. Feasibility study on preparation of fully-waste building blocks using alkali-activated materials to solidify construction and demolition waste residue: Formulation optimization and reaction mechanism. Constr Build Mater. 2024;411:134481. [DOI]
17. Feng D, Zheng J, Gu Y, Liang S. Strength characteristics of South China coastal soft clay solidified by all solid waste geopolymer materials and its durability under dry/wet cycles of loading. Sustain Chem Pharm. 2026;49:102298. [DOI]
18. Lan J, Dong Y, Kai MF, Hou H, Dai JG. Investigation of waste alkali-activated cementing material using municipal solid waste incineration fly ash and dravite as precursors: Mechanisms, performance, and on-site application. J Hazard Mater. 2024;465:133416. [DOI][PubMed]
19. Feng D, Ye F, Chen D, Liang S. Research progress on solidification/stabilization of sludge with Alkali-Activated cementitious materials: A review. Sustain Chem Pharm. 2025;43:101904. [DOI]
20. Tao Y, Sun K, Yang J, Shen B, Zhang Y, Hui D. Influence of calcium oxide and sodium silicate on the setting, hardening and shrinkage properties of alkali-activated slag/fly ash mortars. Constr Build Mater. 2024;453:139104. [DOI]
21. Nath P, Sarker PK. Effect of GGBFS on setting, workability and early strength properties of fly ash geopolymer concrete cured in ambient condition. Constr Build Mater. 2014;66:163-171. [DOI]
22. Xie J, Wang J, Rao R, Wang C, Fang C. Effects of combined usage of GGBS and fly ash on workability and mechanical properties of alkali activated geopolymer concrete with recycled aggregate. Compos Part B Eng. 2019;164:179-190. [DOI]
23. Hou W, Wang J, Feng D, Liang S, Liu F, Wu S. Experimental study on mechanical properties of sodium silicate-activated slag/fly ash solidified South China coastal soft soil. KSCE J Civ Eng. 2025;29(5):100125. [DOI]
24. Zhao G, Guan H, Yan H, Tian J, Han Y, Wang W, et al. Properties and underlying mechanism of flowable solidified shield tunnelling muck: A synergistic approach using slag powder, fly ash and activator. J Environ Chem Eng. 2025;13(6):119990. [DOI]
25. Chen K, Wu D, Zhang Z, Pan C, Shen X, Xia L, et al. Modeling and optimization of fly ash–slag-based geopolymer using response surface method and its application in soft soil stabilization. Constr Build Mater. 2022;315:125723. [DOI]
26. Song Y, Zhang J, Wu H, Yang C, Jia D, Wei W. All-solid-waste alkali-activated materials: A critical review of multi-waste synergy, heavy metal stabilization, and sustainable engineering applications. J Environ Chem Eng. 2025;13(6):119204. [DOI]
27. Huang G, Zhang X, Liu M, Fang B, Wang C, Mi H. Compatibility of sodium hydroxide, sodium silicate and calcium-enriched additives in alkali-activated materials: From the perspectives of flowability, strength and microstructure. Constr Build Mater. 2023;403:133102. [DOI]
28. Xia Y, Shi D, Zhao Y, Wang J, Ma X, Yu K, et al. Designing low-carbon ultra-high performance concrete with co-combustion ash of sewage sludge and rice husk. Mater Struct. 2024;58(1):7. [DOI]
29. Yang Q, Xu W, Yang Y, Liu X, Su Q, Zhang Y, et al. Mechanistic study of the effect of potassium ferrate and straw fiber on the enhancement of strength in cement-based solidified municipal sludge. Sci Rep. 2023;13(1):7660. [DOI][PubMed][PMC]
30. Li X, He C, Lv Y, Jian S, Liu G, Jiang W, et al. Utilization of municipal sewage sludge and waste glass powder in production of lightweight aggregates. Constr Build Mater. 2020;256:119413. [DOI]
31. Cao Y, Lin H, Zong T, Xu X, Li M, Bian X, et al. Strength characteristics and prediction model of solidified municipal sludge reinforced by dredged silt combined with sodium silicate and polyurethane. Sci Rep. 2024;14(1):31947. [DOI][PubMed][PMC]
32. Cristelo N, Glendinning S, Fernandes L, Pinto AT. Effect of calcium content on soil stabilisation with alkaline activation. Constr Build Mater. 2012;29:167-174. [DOI]
33. Shi X, Yang P, Li L, Geng X, Liu X, Zhao J. Strength and microscopic pore structure characterization of cement-fly ash stabilized organic soil under freeze-thaw cycles. Constr Build Mater. 2024;420:135635. [DOI]
34. T/CECS 737-2020. Technical specification for application of road solidified soil. Beijing: China Planning Press; 2020. Chinese. Available from: https://www.gongbiaoku.com/book/h7020022x77
35. Befikadu Zewudie B. Experimental study on the production and mechanical behavior of compressed lime-cement-stabilized interlock soil blocks. Adv Mater Sci Eng. 2023;2023:2933398. [DOI]
36. Huang G, Ji Y, Li J, Zhang L, Liu X, Liu B. Effect of activated silica on polymerization mechanism and strength development of MSWI bottom ash alkali-activated mortars. Constr Build Mater. 2019;201:90-99. [DOI]
37. Habert G, d'Espinose de Lacaillerie JB, Roussel N. An environmental evaluation of geopolymer based concrete production: Reviewing current research trends. J Clean Prod. 2011;19(11):1229-1238. [DOI]

Publisher's Note

Science Exploration remains a neutral stance on jurisdictional claims in published maps and institutional affiliations. The views expressed in this article are solely those of the author(s) and do not reflect the opinions of the Editors or the publisher.